Complex congenital heart disease associated with disordered myocardial architecture in a mid-trimester human fetus

First author's surname: Garcia-Canadilla

Short title: Complex congenital heart disease associated with disordered myocardial architecture

Patricia Garcia-Canadilla, PhD[1,2*] Hector Dejea, MSc,[3,4] Anne Bonnin, PhD[3] Vedrana Balicevic, MSc[5] Sven Loncaric, PhD[5] Chong Zhang, PhD[2] Constantine Butakoff, PhD[2] Jazmin Aguado-Sierra, PhD[6] Mariano Vázquez, PhD[6,7] Laurence H. Jackson, PhD[8] Daniel J. Stuckey, PhD[8] Cristoph Rau, PhD[9] Marco Stampanoni, PhD[3,4] Bart Bijnens, PhD[2,10#] and Andrew C. Cook, PhD[1#]

[1]Institute of Cardiovascular Science, University College London, London, UK

[2]DTIC, Universitat Pompeu Fabra, Barcelona, Spain

[3]Swiss Light Source, Paul Scherrer Institut, Villigen, Switzerland

[4]Institute for Biomedical Engineering, ETH Zurich, Zurich, Switzerland

[5]Faculty of Electrical Engineering and Computing, University of Zagreb, Zagreb, Croatia

[6]Barcelona Supercomputing Center BSC-CNS, Campus Nord UPC, Barcelona, Spain

[7]IIIA / CSIC, Bellaterra, Spain

[8]Centre for Advanced Biomedical Imaging, Division of Medicine, University College London, London, UK

[9]Diamond Manchester Imaging Branchline (I13-2), Diamond Lightsource, Oxford, UK

[10]ICREA, Barcelona, Spain

#Both authors contributed equally to this work

***Address for correspondence:**

Dr Patricia Garcia-Canadilla

UCL Institute of Cardiovascular Science

1st Floor Welcome Trust Building

Institute of Child Health

30 Guilford Street

e-mail: p.canadilla@ucl.ac.uk

Total word count: 5707

ABSTRACT

Background: In the era of increasingly successful corrective interventions in patients with congenital heart disease (CHD) global and regional myocardial remodeling are emerging as important sources of long term morbidity/mortality. Changes in organization of the myocardium in CHD, and in its mechanical properties, conduction and blood supply, result in altered myocardial function both prior to and following surgery. To gain a better understanding and develop appropriate and individualized treatment strategies, the microscopic organization of cardiomyocytes, and their integration at a macroscopic level, need to be completely understood. The aim of this study is to describe, for the first time, in 3D and non-destructively, the detailed remodeling of cardiac micro-structure present in a human fetal heart with complex CHD.

Methods and Results: Synchrotron X-ray Phase-Contrast Imaging (X-PCI) was used to image an archival mid-gestation formalin fixed fetal heart with right isomerism and complex CHD and compare to a control fetal heart. Analysis of myocyte aggregates, at detail not accessible with other techniques, was performed. Macro-anatomical as well as conduction system changes specific to the disease were clearly observable, together with disordered myocyte organization in the morphologically right ventricle (mRV) myocardium. Electrical activation simulations suggested altered synchronicity of the mRV.

Conclusions: We have shown the potential of X-PCI for studying cardiac micro-structure in the developing human fetal heart at high resolution providing novel insight while preserving valuable archival material for future study. This is the first study to show myocardial alterations occur in complex CHD as early as mid-gestation.

INTRODUCTION

Congenital heart disease (CHD) is the leading cause of infant morbidity in developed countries and affects approximately 1% of newborns [1]. For most phenotypes of CHD, effective corrective or palliative interventions have been developed. While an adequate circulation can mostly be established, long term morbidity and mortality is still an important clinical problem, especially those related to heart (myocardial) failure and remodeling. Therefore, beside basic morphology, detailed knowledge of the microarchitecture of the heart and its complex (altered) development is essential, not only for understanding the genesis of CHD and addressing long-term consequences of the disease, but also for developing realistic biophysical computational models as a precursor to new or personalized treatment strategies. Myocytes are aggregated and aligned in a predominant direction within the atrial and ventricular walls, forming a complex three-dimensional network (myocardial architecture). The complex organization of these bundles of myocytes within the myocardium determines the propagation of electrical waves as well as the force development within cardiac tissue. Understanding altered contractile function as well as triggers for remodeling requires knowledge of this organization. Data on the organization of the myocardium in fetal life useful for computational modelling is limited and even our understanding of normal myocardial architecture after birth and in adulthood is still under debate[2,3]. Even less is known about the micro-structure of structurally abnormal hearts, especially given the complexity of CHD and the great variety of underlying phenotypes[4].

Therefore, comparing the organization of the myocardium in different forms of CHD, and quantifying the overall and detailed differences in comparison to normal hearts, is essential for a better understanding of normal and abnormal cardiac architecture, to target long term corrective therapy and to parametrize computational modelling of myocardial development, electrical propagation and resulting function.

In order to identify and quantify cardiac micro-structure and to image the whole heart for evaluating detailed shape and macro-structure, high-resolution imaging (in the order of only a few microns) is required. A number of 3D imaging techniques can be used for assessing detailed cardiac morphology at high resolutions. However, only few of them allow imaging a whole heart volume in 3D non-destructively. Optical (episcopic) microscopy is able to acquire the information needed at high enough contrast and resolution, but is limited to in-vitro imaging and additionally requires the destruction of the sample[5]. High resolution magnetic resonance imaging (MRI) can provide reasonable resolution and contrast for myocardial macro-structure, but to image micro-structure requires the addition of directional sampling in diffusion tensor MRI (DT-MRI), necessitates extremely long scan-times and is still relatively limited in resolution, especially in-vivo[6]. Classical, absorption-based micro-CT shows promise, is fast, has resolution to identify individual cardiomyocytes (in adults) but requires iodine staining to provide adequate contrast[7,8]. Novel high-resolution imaging techniques such as synchrotron X-ray Phase Contrast Imaging (X-PCI) have already demonstrated good results in the study of structural changes of hearts from rabbit fetuses, young rats and human fetuses at μm resolution[9–12], with sufficient contrast to distinguish myocytes at cellular level and without the need for destructive sectioning, tissue processing , or the use of contrast agents.

This study focuses on the detailed analysis of a human fetal heart with complex CHD and a control, as a proof of principle. Specifically, the abnormal heart we analyzed was from a fetus with a defect of laterality, termed isomerism, involving multi-organ abnormalities as well complex CHD. We provide for the first-time details, currently not accessible with other imaging techniques, of the micro-structure of this heart by means of X-PCI, which suggest myocardial abnormalities are indeed present in CHD prior to birth from the mid-trimester of pregnancy. We also show that the accurate measurement of the complex 3D arrangement of

myocytes within the myocardium, together with detailed cardiac geometry, allows detailed computational cardiac electrical activation simulations, providing new insights into functional and electromechanical remodeling in CHD.

METHODS

The data will be made available to other researchers for purposes of reproducing the results[13].

Sample description.

The samples used in this study are from the Cardiac Archive, held at the Institute of Child Health (ICH), under UK Human Tissue Authority Research Licence (N° 12220). The study, including transportation of samples, was approved by the Institute's HTA research committee and the Research committee of the Cardiac Academic Group, Children's Cardiovascular Research Department (GOSH/ICS). First, a heart of 20 weeks of gestation with complex CHD was selected. The selected heart showed right isomerism (bilateral right atrial appendages); a right-sided heart and apex; mirror image arrangement of the ventricles (left-handed ventricular topology or l-loop); atrioventricular septal defect (AVSD) with common atrioventricular junction and valve, pulmonary atresia with aorta from the morphologically right ventricle. In the donating fetus, both lungs were trilobed, bronchi short and eparterial, stomach left-sided, gall-bladder right-sided, liver central, spleen absent, and intestines normally rotated. Prenatal diagnosis at 20 weeks' gestation had shown normal fetal head, brain, face, spine, neck, skin, chest, abdominal wall, gastro-intestinal tract, kidneys and bladder, extremities and skeleton. Image quality was limited but complex CHD was identified comprising right isomerism, right-sided heart and apex, biventricular atrioventricular connection, left hand ventricular topology, unbalanced AVSD with common atrioventricular valve and right ventricular dominance, single outlet with aorta from mRV and pulmonary atresia. Abnormal pulmonary venous Doppler suggested obstruction to pulmonary veins but drainage of pulmonary veins was not clearly identified. There was retrograde flow in the arterial duct and small central pulmonary arteries. The heart was noted to be in sinus rhythm. This amounted to complex CHD with functionally single ventricle and palliative surgery as the likely course postnatally. The parents opted for termination of

pregnancy and consented for autopsy as well as retention of the fetal heart for research purposes.

For comparison, a normal fetal heart of 19 weeks of gestation was chosen from the same historical collection. Notes show termination of pregnancy for social reasons and the fetus had no cardiac or extra-cardiac abnormalities.

Data acquisition

X-ray phase-contrast Imaging

Imaging of the heart with complex CHD heart was performed at the TOMCAT beamline of the Swiss Light Source (SLS, PSI, Switzerland), with X-ray propagation-based phase-contrast tomography, using a 20 keV parallel synchrotron X-ray beam (monochromaticity bandwidth of 2%). The sample was located 60 cm from the detector (camera: sCMOS pco.EDGE 5.5, scintillator: LAG:Ce 300 μm). The field of view (FOV) was 13.03 x 3.2 mm^2 with isotropic pixel size of 5.2 μm. The sample was kept at room temperature placed in a sealed plastic tube with degassed deionized water and secured on a sample holder.

After positioning the heart at the stage's center of rotation, acquisition was performed by rotating the sample through 360º acquiring 2500 projections (exposure time: 70 ms). Nine sequential acquisitions (overlap 126 slices - 0.66 mm) from base to apex, were performed in order to cover the whole heart along its longitudinal axis. Additionally, 50 flat and 20 dark images were acquired for flat-field and dark-field corrections of each acquisition. Before the reconstruction procedure a single-distance phase retrieval approach, the Paganin filter[14], was applied on each projection to improve visualization of the cardiac tissue. The projection set was finally reconstructed, both with and without Paganin filter, using the Gridrec algorithm[15]. Reconstructed volumes were then merged together to obtain a unique single data set for the whole heart with a Matlab script.

The normal heart was scanned at the I13-2 beamline of Diamond Light Source under similar conditions. Briefly, image acquisition was made using a 20 keV parallel synchrotron X-ray beam. The sample was located 120cm from the detector (camera: pco.4000 with a 1.25x objective lens, scintillator: CAWO4 250 µm). The FOV was 14 x 9.6 mm with isotropic pixel size of 3,2 µm. 2001 projections of 0.5s exposure time were recorded. Additionally, 20 flat and 20 dark images were acquired for flat-field and dark-field corrections, applied before the reconstruction procedure. The projection set was reconstructed using the filtered-back projection algorithm.

Magnetic resonance imaging diffusion tensor image

MRI measurements were performed using a 9.4T horizontal bore scanner (Agilent Technologies, Santa Clara, USA) equipped with 1000mT/m gradient inserts and a 26mm volume resonator RF coil (RAPID Biomedical, Rimpar, Germany). 3D fast spin echo DT-MRI acquisition with monopolar diffusion weighting (DW) gradients was performed in the heart with complex CHD (maximum gradient strength = 26G/cm). Acquisition parameters were: isotropic resolution = 156µm, field of view = $2cm^3$, TR/TE = 600/18ms, flip angle 90°, with 3 spatial averages. DW was applied in 30 directions with 3 unweighted b0-volumes, with DW of b = 1180 s/mm^2, gradient strength 0.26T/m, duration 0.5ms and separation 10ms.

Image analysis

Tissue and arterial tree segmentation

Datasets were analyzed with *Fiji* (reslicing/rendering), and image analysis software *Ilastik*[16] (image segmentation). Segmentation of Paganin reconstructed dataset was performed semi-automatically using the two-stage pixel classification module in *Ilastik*. Then, morphological operations were applied to smooth segmentations using first an in-house algorithm implemented in Matlab (R2016b, The MathWorks Inc., Natick, Massachusetts, USA, 2016)

and secondly the *Seg3D* image processing software[17]. Coronary arteries were manually segmented by labelling some slices, then performing a 3D interpolation in *3D Slicer*[18].

Delineation of the conduction tissue

Conduction tissue was visualized as low-density (dark) regions surrounded by connective tissue visible as high-density (bright) areas within the X-PCI images as described in previous studies of normal fetal and postnatal human hearts[11,19]. The obtained dataset was rotated and resliced in Fiji to investigate the cardiac conduction system. In order to improve the visualization of conduction tissue, maximum intensity projection (MIP, depth 5 slices) was performed in the resliced dataset, to improve contrast between differing cardiac tissues. The components of the conduction system including the atrioventricular node (AVN), non-branching, left and right bundle branches were manually traced in *Seg3D* software[17]. 3D interpolation of delineated areas was performed to obtain a 3D volume reconstruction of the whole conduction system in *3DSlicer*[18].

Quantification of the myocyte aggregates orientation

X-ray phase-contrast imaging

The gradient structure tensor was calculated on the reconstructed image dataset without Paganin filter to estimate the local orientation of the myocyte aggregates as described in[10,12]. Briefly, the oriented gradient magnitude in *x*, *y* and *z*-directions were obtained for each voxel using a central difference algorithm. Then, the local structure-tensor within a voxel's cubical neighborhood was calculated. Eigen-decomposition of the structure tensor was performed to transform the given gradient space into a space with three orthogonal vectors. The smallest eigenvalue (λ_3), which indicated the direction with the lowest intensity variation, corresponds to the vector pointing in the myocyte direction, $\mathbf{v}_3$. For the smallest eigenvalues' vector $\mathbf{v}_3$,

the helical angle (HA) α_H was calculated as the angle between the transverse plane and the vector projection to the local tangential plane of the cylindrical coordinate system of the heart (see Supplementary Figure S1a-b).

Detail of the quantification of the HA distribution within both ventricles is provided in section S1 of Supplementary material.

Magnetic resonance imaging diffusion tensor image

Intensity-based thresholding plus manual labelling was performed on baseline images to obtain a mask of the cardiac tissue. The segmented mask was applied to all the DW images. DT-MRI was estimated in the masked volume using Camino[20] with a nonlinear optimization method. Eigenvalues and eigenvectors of the diffusion tensor were computed and the principal eigenvector $\mathbf{v_1}$, describing the main myocyte aggregates direction, was considered to obtain the helical angle, computed as described in the previous section.

Computational modelling of electrical activation

Details about the simulations of the electrical activation propagation are provided in section S1 of Supplementary material.

RESULTS

Visualization of the overall cardiac structure and vasculature

Figure 1 displays example images obtained from the heart with complex CHD, reconstructed using the Gridrec algorithm[15] and the Paganin phase retrieval method[14] showing short axis slices at mid-ventricular (Figure 1a) and atrioventricular valve level (Figure 1b) as well as a longitudinal resliced image through the common atrioventricular valve and apex (Figure 1c). The structure of the three segments of the heart (atria, ventricles and great arteries) can be clearly differentiated and analysed together with sub-structures such as atrioventricular and arterial valvar complexes including fine detail of tendinous cords and valvar leaflets (Figure 1 d-e)).

When visualizing data using volume-rendering (Figure 2 and Supplementary Video 1) the complete structure of the cardiac segments can be identified. Compatible with right isomerism, there are bilaterally extensive pectinate muscles, as seen in short axis (Figure 2c). The ventriculo-arterial connection is also evident, with a patent aortic valve arising from the left-sided mRV and pulmonary atresia. Hypoplastic sinuses are seen within the atretic pulmonary root, which would not be visible by standard techniques of dissection. The type and mode of atrioventricular connection is also clearly seen. There is a biventricular AV connection via a common atrioventricular junction, guarded by a common atrioventricular valve in the setting of an AVSD.

Location of the conduction system in the abnormal fetal heart.

Figure 3 shows the feasibility of manual delineation of the conduction tissue in X-PCI images. Using similar methodology to that used in serial histologic sections[21,22] the conduction system was traced ‘section to section’ through the heart. Dual AVNs were identified, one superiorly and one inferiorly joined by a sling of conduction tissue (common bundle). The connection from the superior AVN to the common bundle was narrower than

the connection inferiorly. The ventricular bundle branches were readily identified arising from the common bundle astride the mid portion of the ventricular septum. Our findings agree with those reported in similar fetal specimens with right isomerism and left-hand topology.[21,22] A 3D reconstruction of the manually delineated conduction system, including both AVNs, common, left and right bundle branches, is shown in Figure 3b and 3c and in Supplementary Video 2.

Myocyte aggregates orientation

A longitudinal plane of the calculated HA of myocyte aggregates together with the visualization of the resulting 3D vector plots within 4 different apical-basal short axis slices of the normal and complex CHD fetal hearts, together with an overall rendering of the resulting 3D fiber structure, are shown in Figure 4. The myoarchitecture of the morphologically left ventricle (mLV) in the abnormal and control hearts show a gradual change in HA from epi- to endocardium as has been showed in adults[23]. However, in the heart with complex CHD, the middle layer of circumferential myocytes is thicker and the deep layer of longitudinal cardiomyocytes thinner compared to the control. Regional areas of more disorganized myocytes are evident in the septal and free wall of the mRV as reflected in the plots of HA within selects slices (Figure 4). Moreover, a flipping of the myocardial pattern within the mid septal wall is evident; myocyte orientation in the apex is normal, but changes to a partially mirror-imaged transmural distribution at the base, similar to that seen in Situs Inversus Totalis[24].

Figure 5 shows the comparison of local helical angles determined by X-PCI (Fig. 5a) and DT-MRI (Fig. 5b) within two slices (apical and mid ventricular). While the overall pattern is qualitatively similar, both show the clear disorganization of myocyte aggregates within the septum and mRV in mid-ventricular slices, the low resolution of DT-MRI images (demonstrated by limited voxels across the lateral wall) makes it more difficult to see the

gradual change in the local HA from endo- to epicardium clearly present in the X-PCI images.

Disorganization in the septum of the isomeric heart is also evident when quantitatively comparing the transmural profiles of HA with the normal control heart (Figure 6), showing a lower linear correlation ($R^2 = 0.81 \pm 0.19$ normal vs. 0.63 ± 0.26 CHD) (Supplementary Table 1).

Finally, according to the distribution of helical angles within the two ventricles (Figure 7), the portion of myocyte aggregates running circumferentially was higher in the complex CHD heart compared to the control; while the mRV in the control heart had approximately 2% less circumferential myocardial strands compared to the mLV the percentage in the complex CHD heart in mRV and mLV are approximately equal (RV = 14.7 ± 0.8 vs LV = 14.0 ± 0.9 %).

DISCUSSION

For the first time, we have non-destructively imaged and quantified the integrated myocardial macro- and micro-structure of a whole ex-vivo human fetal heart with complex CHD. We quantitatively extracted details of 3D micro-anatomy namely cardiac myocyte organization, coronary circulation, and conduction system, and additionally showed how this can be used to (computationally) study the effect of the observed remodeling on electrical activation, as compared to a normal fetal heart.

Our approach shows a proof of principle for X-PCI, and subsequent analysis, to provide a novel promising way for capturing relevant detail of 3D myocyte arrangement and correlating with the conduction system and coronary supply without the need for sample processing, sectioning and image registration. Similar results have been reported in a normal adult heart by means of micro-CT imaging[8] but at approximately 10x lower resolution and requiring iodination of the sample to increase image contrast.

The high-resolution images obtained by X-PCI allow us to discriminate the local predominant direction of myocyte aggregates using a 3D structure tensor approach and, in this initial study, to quantify the transmural distribution of HA . In both complex CHD and control, we observed well-conserved transmural variations in HA from endo- to epicardium in the free wall of the mLV, similar to those reported in human adults or animals[10,12,25]. The wider range of angle values and more regional differences in the HA of myocyte aggregates in comparison to previous studies is likely due to the immature fetal myocardium as well as higher-resolution of our data, allowing us to quantify subtler local changes, as well as the ability to image the trabeculations in more detail. Our results support the hypothesis that cardiomyocytes are aggregated end to end forming a 3D mesh. Our findings show that, even in the midtrimester, there is a smooth change in the HA across the thickness of the mLV rather than the abrupt change in HA that would be expected if the ventricles exist as a unique

myocardial band.[26] Some authors have also described the existence of myocardial "sheets" or "sheetlets". While myocytes undoubtedly clump into linked 'colonies' or 'bunches', we did not find evidence to support myocardial "sheets" in our fetal hearts, albeit that the supporting collagen network is known to be immature at this gestation[27].

In our case with complex CHD and mirror image arrangement of the ventricles our results suggest that there is overall preservation of the change in HA of myocytic aggregates from endo- to epicardium with a circumferential layer within mLV. The mRV is much more disorganized with an extensive deep trabecular layer and smaller circumferential layer. Moreover, while the transmural change in HA of myocyte aggregates in the mLV lateral wall, from endo- to epicardium is quite linear and uniform between all short-axis slices, the septal transmural HA distribution is less linear and more heterogeneous across slices, particularly near the base of the heart. As has been reported in cases of Situs Inversus Totalis[24], we have observed that the orientation pattern of the myocyte aggregates changes from apex to the base, where the superficial (more epicardial) layer of myocyte aggregates in the complex CHD is thinner in the base compared to the apex.

These findings are clinically relevant, since in the abnormal heart, the mLV was noted to be small on prenatal ultrasound. The parents had been counselled of the likelihood of a functionally univentricular palliation being required following birth (the Fontan circulation). In this setting, the mRV would have been the systemic ventricle after corrective surgery. While we cannot predict how the mRV would have developed through subsequent gestation and postnatally, it is well known that patients with right isomerism are particularly difficult to manage following birth and surgery, partly attributed to the constellation of lesions that are present[28]. It is possible that there would have been delayed recovery with normal remodeling of the mRV myocardium later in gestation. However, it is also possible that the regional wall disorganization documented in this heart could persist and that this would lead to very

abnormal regional function and wall stresses, contributing to abnormal global function as well as development of remodeling and fibrosis, thus further contributing to morbidity or mortality.

Finally, our electrophysiological biophysical simulations show the potential of exploiting the high-resolution information retrieved from X-PCI images (detailed geometry integrated with local myocyte orientation) to study cardiac electrical. Similar electrical activation studies have been demonstrated in a normal adult heart by Stephenson et al.[8] Our initial results suggest the presence of electrical dyssynchrony in complex CHD compared to control, likely to lead to further mechanical inefficiency as often observed in CHD. Further delineation of activation following the specific path of the ventricular conduction system could be integrated in order to perform even more accurate and details simulations, but this was out of the scope of this study.

Our study is proof of principle but given the potential value of investigating developmental changes in the myocardium and micro-architecture in CHD, it strongly suggests that a comprehensive survey of fetal hearts with a wide spectrum of disease is warranted.

Limitations might be availability of fetal material and access to time on synchrotrons worldwide but with co-ordination of studies across centres both of these factors could be overcome. With the rapid progress in synchrotron research and further clinical translation it may, in the future, prove possible to perform non-invasive post-mortem imaging of whole fetuses at higher resolutions than other modalities[29,30] and even in-vivo experiments.

Translation of X-PCI to clinical scanners has already begun in the field of mammography for breast cancer detection[31], working towards in-vivo assessment of tissue structure, fibrosis, vessels without the use of contrast agents.

In conclusion, we have shown the potential of synchrotron X-PCI, to demonstrate macro- and micro-anatomy of human fetal hearts in 3D, preserving invaluable research material for

further study, and allowing detailed co-characterization of the myocardium, coronaries and conduction system thus providing novel, clinically relevant insight into the structure of fetal hearts with CHD.

ACKNOWLEDGMENTS

We acknowledge the Paul Scherrer Institut, Villigen, Switzerland and Diamond Light Source, Oxford (UK) for provision of synchrotron radiation beamtime at beamline X02DA TOMCAT and at beamline I13-2 respectively. PGC acknowledges EMBO for a short-term fellowship at the Paul Scherrer Institute (PSI), Villigen, Switzerland and Fundació Daniel Bravo Andreu for a research fellowship at UCL London.

SOURCES OF FUNDING

This study was partially supported by the Spanish Ministry of Economy and Competitiveness (grant TIN2014-52923-R and the Maria de Maeztu Units of Excellence Programme - MDM-2015-0502) and FEDER. CB is supported by Fundació La Marató de TV3 (Spain), grant Nº: 20154031. JAS is supported by the Center of Excellence CompBioMed funded under H2020-EU.1.4.1.3. under grant agreement Nº 675451.

DISCLOSURES

None

REFERENCES

1. Dolk H, Loane M, Garne E, European Surveillance of Congenital Anomalies (EUROCAT) Working Group. Congenital Heart Defects in Europe: Prevalence and Perinatal Mortality, 2000 to 2005. *Circulation*. 2011;123:841–849.
2. Anderson RH, Smerup M, Sanchez-Quintana D, Loukas M, Lunkenheimer PP. The three-dimensional arrangement of the myocytes in the ventricular walls. *Clin Anat*. 2009;22:64–76.
3. Torrent-Guasp F, Ballester M, Buckberg GD, Carreras F, Flotats A, Carrió I, Ferreira A, Samuels LE, Narula J. Spatial orientation of the ventricular muscle band: Physiologic contribution and surgical implications. *J Thorac Cardiovasc Surg*. 2001;122:389–392.
4. Henderson DJ, Anderson RH. The development and structure of the ventricles in the human heart. *Pediatr Cardiol*. 2009;30:588–96.
5. Matsui H, Mohun T, Gardiner HM. Three-dimensional reconstruction imaging of the human foetal heart in the first trimester. *Eur Heart J*. 2010;31:415–415.
6. Mekkaoui C, Porayette P, Jackowski MP, Kostis WJ, Dai G, Sanders S, Sosnovik DE. Diffusion MRI tractography of the developing human fetal heart. *PLoS One*. 2013;8:e72795.
7. Stephenson RS, Boyett MR, Hart G, Nikolaidou T, Cai X, Corno AF, Alphonso N, Jeffery N, Jarvis JC. Contrast enhanced micro-computed tomography resolves the 3-dimensional morphology of the cardiac conduction system in mammalian hearts. *PLoS One*. 2012;7:e35299.
8. Stephenson RS, Atkinson A, Kottas P, Perde F, Jafarzadeh F, Bateman M, Iaizzo PA, Zhao J, Zhang H, Anderson RH, Jarvis JC, Dobrzynski H. High resolution 3-Dimensional imaging of the human cardiac conduction system from microanatomy to

mathematical modeling. *Sci Rep*. 2017;7.

9. Mirea I, Varray F, Zhu YM, Fanton L, Langer M, Jouk PS, Michalowicz G, Usson Y, Magnin IE. Very high-resolution imaging of post-mortem human cardiac tissue using X-ray phase contrast tomography. In: Functional Imaging and Modeling of the Heart. Springer International Publishing; 2015. p. 172–179.

10. Gonzalez-Tendero A, Zhang C, Balicevic V, Cárdenes R, Loncaric S, Butakoff C, Paun B, Bonnin A, Garcia-Cañadilla P, Muñoz-Moreno E, Gratacós E, Crispi F, Bijnens B, Cardenes R, Loncaric S, Butakoff C, Paun B, Bonnin A, Garcia-Cañadilla P, Muñoz-Moreno E, Gratacos E, Crispi F, Bijnens B. Whole heart detailed and quantitative anatomy, myofibre structure and vasculature from X-ray phase-contrast synchrotron radiation-based micro computed tomography. *Eur Hear J - Cardiovasc Imaging*. 2017;18:732–741.

11. Kaneko Y, Shinohara G, Hoshino M, Morishita H, Morita K, Oshima Y, Takahashi M, Yagi N, Okita Y, Tsukube T. Intact Imaging of Human Heart Structure Using X-ray Phase-Contrast Tomography. *Pediatr Cardiol*. 2017;38:390–393.

12. Baličević V, Lončarić S, Cárdenes R, Gonzalez-Tendero A, Paun B, Crispi F, Butakoff C, Bijnens B. Assessment of Myofiber Orientation in High Resolution Phase-Contrast CT Images. Springer, Cham; 2015. p. 111–119.

13. Cook AC. Cardiac Morphology. http://www.cardiacmorphology.com/. 2018;

14. Paganin D, Mayo SC, Gureyev TE, Miller PR, Wilkins SW. Simultaneous phase and amplitude extraction from a single defocused image of a homogeneous object. *J Microsc*. 2002;206:33–40.

15. Marone F, Stampanoni M. Regridding reconstruction algorithm for real-time tomographic imaging. *J Synchrotron Radiat*. 2012;19:1029–1037.

16. Sommer C, Sträehle C, Köthe U, Hamprecht FA. Ilastik: Interactive learning and

segmentation toolkit. In: Proceedings - International Symposium on Biomedical Imaging. IEEE; 2011. p. 230–233.

17. Cibc. Seg3D: Volumetric Image Segmentation and Visualization. Scientific Computing and Imaging Institute (SCI), Download from: http://www.seg3d.org. 2013;

18. Fedorov A, Beichel R, Kalpathy-Cramer J, Finet J, Fillion-Robin J-C, Pujol S, Bauer C, Jennings D, Fennessy F, Sonka M, Buatti J, Aylward S, Miller J V, Pieper S, Kikinis R. 3D Slicer as an image computing platform for the Quantitative Imaging Network. *Magn Reson Imaging*. 2012;30:1323–41.

19. Shinohara G, Morita K, Hoshino M, Ko Y, Tsukube T, Kaneko Y, Morishita H, Oshima Y, Matsuhisa H, Iwaki R, Takahashi M, Matsuyama T, Hashimoto K, Yagi N. Three Dimensional Visualization of Human Cardiac Conduction Tissue in Whole Heart Specimens by High-Resolution Phase-Contrast CT Imaging Using Synchrotron Radiation. *World J Pediatr Congenit Hear Surg*. 2016;7:700–705.

20. Cook PA, Bai Y, Nedjati-Gilani S, Seunarine KK, Hall MG, Parker GJ, Alexander DC. Camino: Open-Source Diffusion-MRI Reconstruction and Processing. In: 14th Scientific Meeting of the International Society for Magnetic Resonance in Medicine. 2006. p. 2759.

21. Smith A, Yen Ho S, Anderson RH, Connell MG, Arnold R, Wilkinson JL, Cook AC. The diverse cardiac morphology seen in hearts with isomerism of the atrial appendages with reference to the disposition of the specialised conduction system. *Cardiol Young*. 2006;16:437.

22. Ho SY, Fagg N, Anderson RH, Cook A, Allan L. Disposition of the atrioventricular conduction tissues in the heart with isomerism of the atrial appendages: its relation to congenital complete heart block. *J Am Coll Cardiol*. 1992;20:904–10.

23. Anderson RH, Ho SY, Redmann K, Sanchez-Quintana D, Lunkenheimer PP. The

anatomical arrangement of the myocardial cells making up the ventricular mass. *Eur J Cardiothorac Surg*. 2005;28:517–25.

24. Delhaas T, Kroon W, Decaluwe W, Rubbens M, Bovendeerd P, Arts T. Structure and torsion of the normal and situs inversus totalis cardiac left ventricle. I. Experimental data in humans. *AJP Hear Circ Physiol*. 2008;295:H197–H201.

25. Teh I, Burton RAB, McClymont D, Capel RA, Aston D, Kohl P, Schneider JE. Mapping cardiac microstructure of rabbit heart in different mechanical states by high resolution diffusion tensor imaging: A proof-of-principle study. *Prog Biophys Mol Biol*. 2016;121:85–96.

26. MacIver DH, Stephenson RS, Jensen B, Agger P, Sánchez-Quintana D, Jarvis JC, Partridge JB, Anderson RH. The end of the unique myocardial band: Part I. Anatomical considerations. *Eur J Cardio-Thoracic Surg*. 2018;53:112–119.

27. Jackson M, Connell MG, Smith A. Development of the collagen network of the human fetal myocardium: an immunohistochemical study. *Int J Cardiol*. 1993;41:77–86.

28. Graupner O, Enzensberger C, Wieg L, Willruth A, Steinhard J, Gembruch U, Doelle A, Bahlmann F, Kawecki A, Degenhardt J, Wolter A, Herrmann J, Axt-Fliedner R, Fetal Cardiac Imaging Research Group Germany. Evaluation of right ventricular function in fetal hypoplastic left heart syndrome by color tissue Doppler imaging. *Ultrasound Obstet Gynecol*. 2016;47:732–738.

29. Arthurs OJ, Thayyil S, Olsen OE, Addison S, Wade A, Jones R, Norman W, Scott RJ, Robertson NJ, Taylor AM, Chitty LS, Sebire NJ, Owens CM, Magnetic Resonance Imaging Autopsy Study (MaRIAS) Collaborative Group. Diagnostic accuracy of post-mortem MRI for thoracic abnormalities in fetuses and children. *Eur Radiol*. 2014;24:2876–84.

30. Lombardi CM, Zambelli V, Botta G, Moltrasio F, Cattoretti G, Lucchini V, Fesslova

V, Cuttin MS. Postmortem microcomputed tomography (micro-CT) of small fetuses and hearts. *Ultrasound Obstet Gynecol*. 2014;44:600–609.

31. Castelli E, Tonutti M, Arfelli F, Longo R, Quaia E, Rigon L, Sanabor D, Zanconati F, Dreossi D, Abrami A, Quai E, Bregant P, Casarin K, Chenda V, Menk RH, Rokvic T, Vascotto A, Tromba G, Cova MA. Mammography with synchrotron radiation: first clinical experience with phase-detection technique. *Radiology*. 2011;259:684–94.

FIGURE LEGENDS

Figure 1. X-ray phase contrast synchrotron radiation-based micro-CT imaging of complex CHD. Short axis (a)-(b) and a longitudinal resliced images (c) showing detail of papillary muscles (a), common atrioventricular valve (b,c), aortic and tricuspid valves (d), the aorta and pulmonary trunk (e). mLV, mRV: morphologically left and right ventricles respectively; AVSD: Atrioventricular septal defect.

Figure 2. Detailed visualisation of cardiac anatomy and vasculature. (a) Volume rendered image depicting detailed cardiac anatomy together with proximal coronary tree (red). (b) Longitudinal and (c) short-axis virtual cuts of the 3D volume render showing details of abnormal anatomy including AVSD, extensive pectinate muscles and atretic pulmonary valve. mLA, mRA: morphologically left and right atriums respectively.

Figure 3. **Delineation and 3D reconstruction of the conduction system in complex CHD**. (a) Virtual longitudinal cut of the resliced X-PCI dataset showing delineation of the conduction tissue (dashed green line). (b) Maximum intensity projection of the X-PCI dataset together with 3D rendering showing two AVNs connected by a sling of conduction tissue (green). (c) Volumetric reconstruction and 3D representation of the conduction system (green) showing the common, left and right bundle branches. Sup. AVN and Inf. AVN: superior and inferior atrioventricular nodes respectively.

Figure 4. **Quantification of helical angle in fetal hearts.** Longitudinal slice of the local helical angle (HA) of myocyte aggregates together with representation of the 3D HA vectors in four short-axis slices of both (a) normal and (b) complex CHD fetal hearts at different apical-basal positions. (c) From left to right: lateral left ventricle (LV), anterior, lateral right

ventricle (RV), posterior and apical views of the fetal heart with tracking based on $\mathbf{v_3}$ eigenvector. Tracks were colour-coded by z-component value of the unit $\mathbf{v_3}$ vector.

Figure 5. **Comparison between X-PCI and DT-MRI helical angle analysis**. Estimation of helical angle (HA) in two different apical-basal image slices with (a) X-PCI and (b) DT-MRI analysis. All images were colour-coded by HA value.

Figure 6. **Transmural variation in helical angle.** Left ventricular transmural profiles of helical angles across four segments (lateral, septal, anterior and posterior) in four different slices (apical, mid-low, mid-high and basal) in the (a-d) normal and (e-h) complex CHD fetal heart.

Figure 7. **Histograms of helical angle in LV and RV of fetal hearts**. Histograms of helical angle for the left (LV) and right ventricles (RV) in four slices (apical, mid-low, mid-high and basal) in the (a-d) normal and (e-h) complex CHD fetal hearts.

Supplementary material

S1. Supplementary methods

Quantification of the myocyte aggregates orientation

X-ray phase-contrast imaging

To quantify the helical angle distribution within the LV and RV, first LV and RV were manually delineated in the different short-axis planes. Then, histograms of the helical angle distribution within each ventricle were computed across five adjacent apical, mid-low, mid-high and basal ventricular slices with a bin size of 2º. The percentage of circumferential arranged myocyte aggregates was calculated by considering only the myocyte aggregated with a helical angle within the range of [-10º,10º]. To assess the local differences of the transmural profiles of myocyte aggregates orientation in different regions of interested (ROI) within the LV, segments of LV myocardium of 20º wide in short-axis plane were defined as the LV lateral, septal, anterior and posterior walls, as previously done in other similar studies[1] (see Supplementary Figure S1). The transmural profiles of the helical angle were calculated for each ROI in the apical, mid-low, mid-high and basal slices. To do so, transmural profiles of helical angle, corresponding to each ROI, were averaged in polar coordinates. Then, the profiles were plotted as a function of normalized wall thickness from endo-to epicardium. Phase wrapping of the helical angle around +90º, as occurring particularly in the papillary muscles region, was avoided by expanding the dynamic range to +150º to -90º. A linear regression fitting was performed to the different transmural profiles to characterize their linearity. R2 coefficient and gradient over the myocardial wall in º/mm were computed. All processing was performed using in-house code developed in Matlab. Finally, 3D fiber tracking was performed in the whole heart along vector v3 in Paraview[2], using a 2nd order Runge-Kutta method. Tracks were displayed in the whole heart and color-coded by z-component of the v3 eigenvector.

Computational modelling of electrical activation

The segmentation datasets created from the X-PCI images of both normal and abnormal fetal hearts were subsampled four times along every axis. Subsequently, VTK[3] was used to construct the corresponding hexahedral meshes, where every voxel was transformed into a hexahedron, resulting in 25.5 and 40.5 million elements with edge length of 41.6um and 18.8um respectively. The local orientation of myocytes aggregates calculated previously was assigned to every vertex of the 3D meshes.

The electrical activation simulations were carried out using the monodomain approximation of electrophysiology using Alya, the Barcelona Supercomputing Center (BSC)'s in-house, multi-physics, HPC solver[4–6] on the MareNostrum 4 supercomputer on 432 high memory processors (RRID:SCR_015737), at the BSC. The diffusion was assumed equal to half the diffusion of a normal adult myocardium[7] and the ionic cell model employed was the human myocyte model published by Ohara[8] assuming all cells have an endocardial action potential. The simulations were initialized by activating the whole endocardial surface.

S2. Supplementary results

Electrical activation simulations

The complex organization of the bundles of myocytes within the myocardium guides the propagation of the electrical waves as well as the force development within cardiac tissue. Therefore, in order to perform etiology- or individual-specific electrophysiological simulations, the specific orientation of myocyte aggregates have to be mapped to the subject-specific volumetric anatomy. The results of the electrical activation simulations performed in both hearts are summarized in Supplementary Figure 2, Supplementary Table 2 and Supplementary Video 3. Supplementary Figure 2a-c show the cumulative histograms for the control and abnormal hearts normalized by the tissue volume and the isochrones maps of electrical wave propagation of both hearts are displayed in Supplementary Figure 2d. While the complex CHD heart might be activated faster per volume unit, there is a clear heterogeneity in activation, where both the synchronicity of RV versus LV, as well as the homogeneous propagation within one ventricle, is hampered due to the myocytes disorganization within the septum and RV.

S3. Supplementary figures

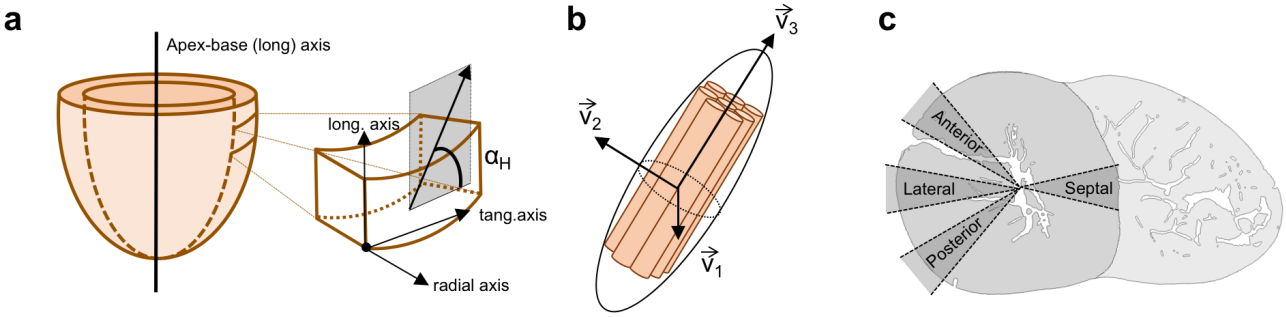

Supplementary Figure 1. Definition of eigenvectors, angles, and segments. (a) Cardiac cylindrical coordinates and angle system used to describe myocyte aggregates orientation is defined with radial, tangential (tang.) and longitudinal (long.) axis. The helical angle (α_H) is defined as the angle between the short-axis plane and the projection of principal orientation onto the tangential-longitudinal plane. (b) Scheme of the coordinates system defined with eigenvectors ($\mathbf{v_i}$, i=1…3) obtained with structure tensor analysis. (c) Specification of regions-of-interest in the left ventricle (LV): lateral, anterior, posterior and septal walls.

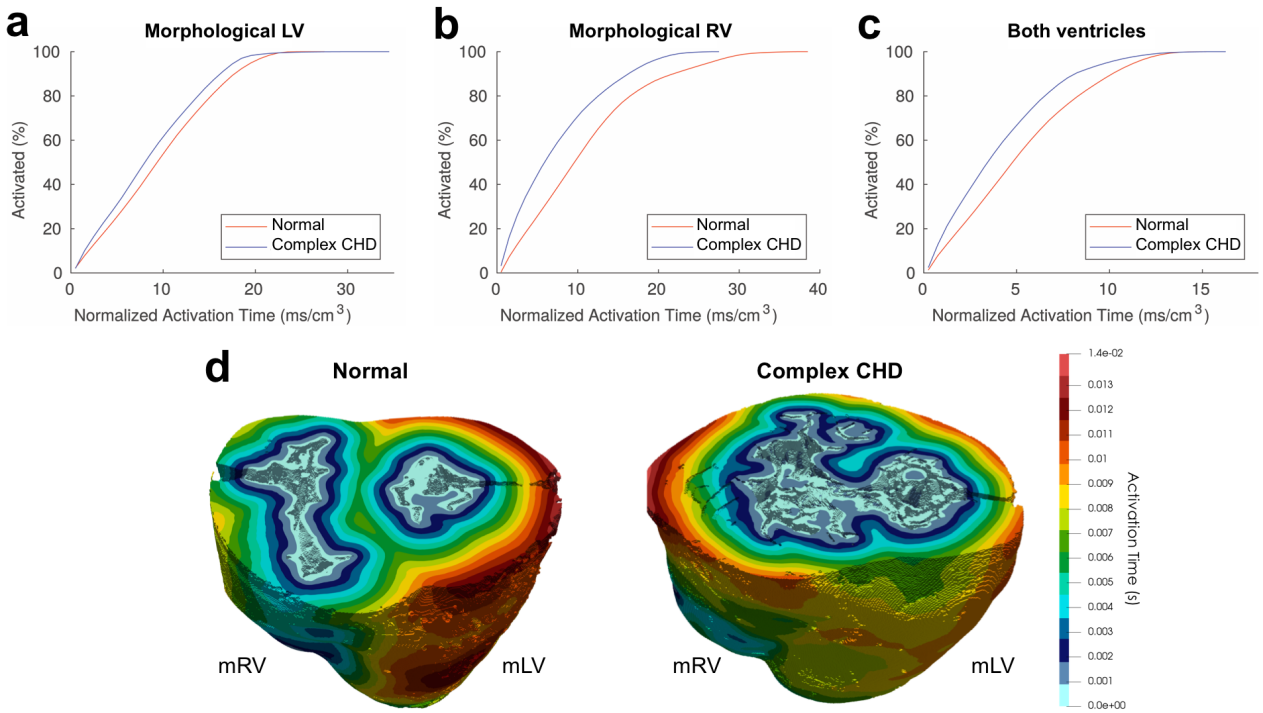

Supplementary Figure 2. **Activation times and isochrone maps of cardiac depolarization seeded from the endocardium**. Cumulative histograms of activation time in the (a) morphologically left ventricle (mLV), (b) morphologically right ventricle (mRV) and (c) in both ventricles in the normal (red) and in the complex CHD (blue) fetal hearts. (d) Isochrone maps of cardiac depolarization in both normal (left) and complex CHD (right) fetal hearts.

S4. Supplementary Tables

Supplementary Table 1. Linearity (R^2 of the linear regression fitting) and gradient of transmural $\mathbf{v_3}$ helical angle profiles in apical, mid-low, mid-high and basal myocardial slices in lateral, septal, anterior and posterior walls in the normal and complex CHD fetal hearts. Linearity and gradient were measured from the LV endocardium to epicardium.

		Lateral		**Septal**		**Anterior**		**Posterior**	
		Linearity	**Gradient (°/mm)**	**Linearity**	**Gradient (°/mm)**	**Linearity**	**Gradient (°/mm)**	**Linearity**	**Gradient (°/mm)**
Normal	**Apical**	0.97	-56.29	0.91	-46.00	0.99	-51.25	0.99	-47.67
	Mid-low	0.99	-39.21	0.84	-39.77	0.97	-43.50	0.99	-42.87
	Mid-high	0.93	-27.30	0.54	-42.55	0.97	-35.05	0.94	-30.42
	Basal	0.99	-38.07	0.96	-47.30	0.99	-42.97	0.87	-36.69
Complex CHD	**Apical**	0.88	-36.66	0.73	-31.30	0.70	-36.89	0.885	-43.82
	Mid-low	0.96	-47.07	0.82	-59.67	0.88	-38.51	0.944	-44.90
	Mid-high	0.87	-47.37	0.24	-24.69	0.94	-44.57	0.954	-51.69
	Basal	0.95	-50.61	0.72	-33.99	0.94	-40.57	0.838	-45.28

Supplementary Table 2. Activation times obtained from the electrophysiological simulations in both normal and abnormal fetal hearts.

Activation times normalised by volume	**Normal**	**Abnormal**
Left Ventricle (LV) (s/cm^3)	0.0159	0.0133
Right Ventricle (RV) (s/cm^3)	0.0157	0.0187
Septum (s/cm^3)	0.0073	0.0044
LV basal (s/cm^3)	0.0157	0.0097
RV basal (s/cm^3)	0.0096	0.0138
LV-Septum difference (s/cm^3)	0.0084	0.0054
RV-Septum difference (s/cm^3)	0.0023	0.0094

S5. Supplementary Videos

Supplementary Video 1. Top to bottom swept of the volumetric rendered image of the complex CHD fetal heart.

Supplementary Video 2. Volumetric render of the delineated conduction system together with a subvolume of the X-PCI dataset of the complex CHD fetal heart.

Supplementary Video 3. Electrical wave propagation in the complex CHD (left) and in the normal (right) fetal heart. Colours indicated activation time.

REFRENCES

1. Teh I, Burton RAB, McClymont D, Capel RA, Aston D, Kohl P, Schneider JE. Mapping cardiac microstructure of rabbit heart in different mechanical states by high resolution diffusion tensor imaging: A proof-of-principle study. *Prog Biophys Mol Biol*. 2016;121:85–96.
2. Ahrens J, Geveci B, Law C. ParaView: An end-user tool for large-data visualization. In: Visualization Handbook. 2005. p. 717–732.
3. Schroeder WJ, Martin KM. The Visualization Toolkit. In: Visualization Handbook. Elsevier; 2005. p. 593–614.
4. Vázquez M, Arís R, Houzeaux G, Aubry R, Villar P, Garcia-Barnés J, Gil D, Carreras F. A massively parallel computational electrophysiology model of the heart. *Int j numer method biomed eng*. 2011;27:1911–1929.
5. Santiago A, Aguado-Sierra J, Zavala M, Doste-Beltran R, Gomez S, Arís R, Houzeaux G, Vásquez M. Fluid-electro-mechanical model of the human heart for supercomputerstle. *Int j numer method biomed eng*. 2017;Submitted.
6. Santiago A, Aguado-Sierra J, Arís S, Casoni E, Lopez-Yunta M, Rivero M, Sacco F, Houzeaux G, Vázquez M. Clinical and Industrial applications with a fluid-electro-mechanical model of the human heart. *Front Physiol*. 2017;Submitted.
7. Bueno-Orovio A, Cherry EM, Fenton FH. Minimal model for human ventricular action potentials in tissue. *J Theor Biol*. 2008;253:544–560.
8. O'Hara T, Virág L, Varró A, Rudy Y. Simulation of the Undiseased Human Cardiac Ventricular Action Potential: Model Formulation and Experimental Validation. *PLoS Comput Biol*. 2011;7:e1002061.